Ion Selectivity and Competition in Channelrhodopsins

Franziska Schneider,[†*] Dietrich Gradmann,[‡] and Peter Hegemann[†]
[†]Institute of Biology, Experimental Biophysics, Humboldt-Universität zu Berlin, Berlin, Germany; and [‡]A.-v.-Haller-Institut der Universität, Göttingen, Germany

ABSTRACT Channelrhodopsins are light-gated ion channels of green algae. They are widely used for the analysis of neuronal networks using light in the emerging field of optogenetics. Under steady-state light conditions, the two open states, O1 and O2, mediate the photocurrents with different ion conductance and selectivity. To understand the conducting process as well as its optogenetic applications, it is important to study ion binding and transport of this promiscuous cation channel. Here, we present an enzyme kinetic algorithm that allowed us to calculate the ion composition of the initial and steady-state photocurrents for multication media. The approach is based on current-voltage relations determined for the individual ions H^+, Na^+, Ca^{2+}, and Mg^{2+}. We identify and quantify the widely different competition of the ions in wild-type channelrhodopsin-2 and two high-performing channelrhodopsin variants CatCh+ and C1V1. Both variants show enhanced Ca^{2+} conductance, but only CatCh+ displays high steady-state Ca^{2+} currents at neutral pH due to reduced H+ competition and low inactivation. We demonstrate that for optogenetic applications, one should always take into account that the variable equilibria of the two open states depend on light intensity, voltage, and the ionic composition of the medium.

INTRODUCTION

Channelrhodopsins (ChRs) are light-gated ion channels that initiate photoreception in phototactic algae such as *Chlamydomonas reinhardtii* and *Volvox carteri*. When activated by light, ChRs depolarize the plasma membrane by conducting protons as well as monovalent (Na^+, K^+) and divalent cations (Ca^{2+}, Mg^{2+}) (1,2). ChRs are widely used in neuroscience to activate specific cells of neuronal networks and trigger action potentials using light (optogenetics). ChR2 of *Chlamydomonas reinhardtii* was the first ChR applied in neuronal cells in 2005 (3–5) and has since developed as the predominant optogenetic tool. To understand ChR-mediated photocurrents in both algae and host model systems, a profound understanding of their kinetics and current-voltage relationships $I(E)$ is crucial.

In response to low-intensity rectangular light pulses, the currents rise nearly monoexponentially to a steady-state level and decline biexponentially back to zero after light-off. However, the current rise is faster at increasing light intensities and the photocurrents display peak currents that temporally relax to steady-state photocurrents of reduced amplitude. Fig. 1 *A* depicts the typical current trace of ChR2, indicating the initial current I_0 determined by extrapolation of the peak current to time zero of illumination and the steady-state current I_s. The relaxation from I_0 to I_s with the time constant τ is commonly referred to as inactivation, and the apparent peak is called the transient current. This inactivation depends on the membrane voltage and ion composition of the internal and external medium. The ratio I_0/I_s and the time constant τ serve as characteristic parameters for the inactivation event. Moreover, I_s saturates at lower light intensities than I_0. The nonmatching light dependence of initial and steady-state currents was originally explained by two alternative schemes: first by a population of late nonconducting photocycle intermediates and, second, by the existence of two open states (6).

The minimal photocycle model comprises two open states O1 and O2 in equilibrium, and two closed states C2 and C1 with a nonreversible transition from C2 to C1 (Fig. 1 *B*). The conductance of O2 was assumed to be lower than of O1 in this model (6–8). Activation of a dark-adapted ChR first results in an initial channel conductance that can be exclusively assigned to O1, which transitions into a stationary conductance with contributions from both O1 and O2. The equilibrium between O1 and O2 is determined by the voltage, extracellular pH (pH_e), and the intensity and color of the actinic light. A careful analysis of the reversal voltages E_r under different ionic conditions revealed that the conductance and ion selectivity differ between O1 and O2 (9). However, the relative contribution of various ions to the steady-state photocurrents in complex media at neutral pH remained uncertain. To overcome this limitation and quantitatively describe the cation transport by various ChRs in the presence of different electrochemical gradients, we have applied a general enzyme-kinetic model with a single predominant ion binding site (10).

The previously used four-state model (Fig. 1 *C*) considers a binding site E that can switch its orientation between the extracellular (*e*) and cytosolic (*c*) sides. Switching can occur in the empty and loaded binding site, yielding four corresponding states E_c, E_e, ES_c, and ES_e. The charge of the empty binding site, z_E, is essential for the voltage sensitivity of the system (11). Considering only external changes of

Submitted March 5, 2013, and accepted for publication May 20, 2013.

*Correspondence: schneifr@hu-berlin.de

Editor: Randall Rasmusson.

0006-3495/13/07/0091/10 $2.00

http://dx.doi.org/10.1016/j.bpj.2013.05.042

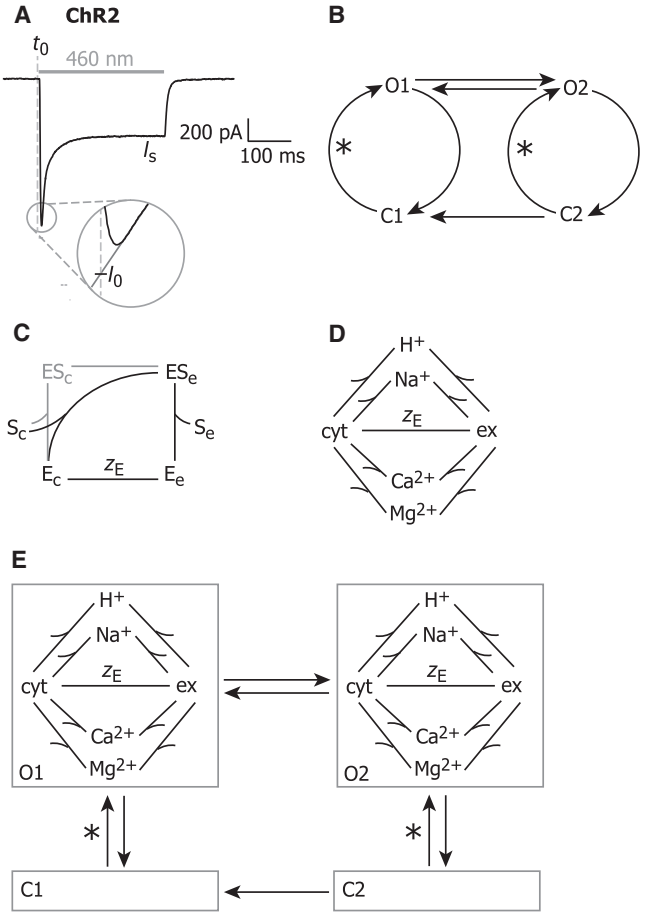

FIGURE 1 Background information. (*A*) Typical photocurrent trace of ChR2 upon stimulation by 460-nm light for 300 ms (100%). The initial current I_0 is determined by linear extrapolation to $I(t = 0)$. (*B*) ChR photocycle model with two serial open states, O1 and O2, and two closed states, C1 and C2. (*C*) Reaction scheme for translocation of an ionic substrate (S) by an enzyme (E) with an apparent charge number (z_E) in its empty state. (*Shaded*) Explicit four-state model; (*solid*) three-state model used here for parameter identification from experimental $I(E)$ curves with only external changes of substrate concentration. (*D*) Reaction scheme for four competing substrates and external concentration changes of protons (H^+), Na^+ (meaning Na^+ or K^+), Ca^{2+}, and Mg^{2+}. (*E*) Consideration of two open states results in two distinct reaction schemes.

substrate concentrations here, cytoplasmic binding/dissociation and reversible orientation are unified into one reversible step, reducing the number of free parameters for each substrate by two. In a previous study, we explicitly calculated transport rates for three types of substrates; protons, monovalent (Na^+/K^+), and divalent cations (Ca^{2+}/Mg^{2+}) and obtained a set of rate constants that allowed the description of the current-voltage relation of I_0 in various ionic conditions (10).

The current study extends our model to four substrates (protons, Na^+, Ca^{2+}, and Mg^{2+}) and considers both open states O1 and O2. The substrates compete for binding to and transport through the channel, which is implemented in the model by substrate-specific three-state transport cycles that share the reorientation of the empty binding site (Fig. 1 *D*). K^+ is not considered in this approach, but may be treated equivalent to Na^+ with similar binding and transport properties (2,12,13). Ca^{2+} and Mg^{2+} show considerably different transport rates and are treated independently. Whereas earlier models focused on the initial current I_0, our model includes both I_0 and the steady-state current I_s. Considering both open states O1 and O2 leads to the reaction scheme in Fig. 1 *E*, where the two open states of Fig. 1 *B* are specified by a particular transport reaction scheme. This model enables us to dissect the currents into the contributions of all four competing ionic species for a set of measured $I(E)$ curves. Furthermore, the model allows for the calculation of current sizes at ionic conditions that were not explicitly tested in experiments.

MATERIALS AND METHODS

Molecular biology

Human codon-adapted C1V1-A and ChR2-LC-TC genes were cloned into peCFP-N1 and p-mCherry-N1 as described by Prigge et al. (14).

HEK cell recording

HEK293 cells were cultured as described in Berndt et al. (9) and seeded onto coverslips at a density of 1.25×10^5 cells·mL^{-1} and supplemented with 1 μM all *trans*-retinal. Transient transfection was performed using Fugene HD (Roche, Mannheim, Germany) 20–48 h before measurements. For ChR2 measurements, a cell line stably expressing ChR2-mVenus was used (15). Whole-cell patch-clamp measurements were performed and signals were amplified and digitized using AxoPatch200B (Axon Instruments, Molecular Devices, Sunnyvale, CA) and DigiData1400 (Molecular Devices). Light activation was achieved using a 75-W Xenon Arc Lamp (Leistungselektronik, Jena, Germany) coupled into the optical path of an Axiovert 35 inverted microscope (Carl Zeiss, Jena, Germany) and regulated by a programmable shutter system. Wavelengths were selected via the following set of filters: BP546 ± 15 nm for C1V1 and BP470 ± 20 nm for ChR2 variants resulting in light intensities of 0.68 mW·mm^{-2} at 546 ± 15 nm and 1.71 mW·mm^{-2} at 470 ± 20 nm (100%) in the object plane, respectively. Buffer composition for ion selectivity measurements is summarized in Table 1. All buffers were pH-adjusted with *n*-methyl-D-glucamine (NMG) or HCl and the final osmolarity was brought to 320 mOsm (extracellular solutions) or 290 mOsm (intracellular solutions) using glucose.

Data analysis

Data were analyzed using the softwares CLAMPFIT 10.2 (Molecular Devices), EXCEL 2007 (Microsoft, Redmond, WA) and SIGMAPLOT 11 (Systat Software, San Jose, CA). From all complete data sets, the ones with best concordance between pre- and postcontrol at standard conditions (140 mM NaCl, pH_e 7.2) were selected. Current amplitudes were normalized to I_0 (−60 mV) at standard conditions (I_{0ref}), and possible drifts were eliminated by temporal interpolation between pre- and postcontrol.

To calculate the four partial ionic currents through each of the two conducting states we used the reaction scheme as depicted in Fig. 1 *E*. Basically, we applied the algorithms of Klieber and Gradmann (16) and Gradmann et al. (10) with some modifications. First, the formalism was extended from three ion species H (H^+), M (Na^+, K^+), and D (Ca^{2+}) to four ionic species by implementing G (Mg^{2+}) as well.

TABLE 1 Summary of buffer compositions

	Extracellular buffer [mM]						Intracellular buffer [mM]
Buffer	140 mM Na^+ pH_e 7.2/ 9.0	2 mM Ca^{2+} pH_e 9.0	20 mM Ca^{2+} pH_e 9.0	70 mM Ca^{2+} pH_e 7.2/ 9.0	20 mM Mg^{2+} pH_e 9.0	70 mM Mg^{2+} pH_e 9.0	NMG pH_c 7.2/ 9.0
NaCl	140	1	1	1	1	1	1
KCl	1	1	1	1	1	1	1
$CaCl_2$	2	2	20	70[a]	2	2	2
$MgCl_2$	2	2	2	2	20	70[b]	2
NMG[a]	—	140	100	—	100	—	110
HEPES/Tris-HCl	10	10	10	10	10	10	10
EGTA	—	—	—	—	—	—	10

[a]NMG, *n*-methyl-D-glucamine. It is used as a Na^+ substitute in systems to maintain physiological solutions as isotonic, but without sodium.
[b]To achieve an equal number of positive charges available for transport, 140 mM Na^+ is replaced by 70 mM Ca^{2+} or Mg^{2+}.

In more detail: To calculate the steady-state currents of the model, the probabilities of the state occupancies p have to be determined. This can be done with the method of King and Altman (17) by forming the relative occupation probabilities $\underline{p}$, that consist of the sum of all products of $n-1$ rate constants in a n-state model. Using the abbreviation $\kappa_S = k_{Sc} + k_{Se}$ (S: H, M, D, or G) for writing economy, these relative occupation probabilities for a given conducting state (O1 or O2) in our six-state model (Fig. 1 *D*) are given by the following equations:

$$\underline{p}_e = k_{ec}\,\kappa_H\kappa_M\kappa_D\kappa_G + k_{eH}\,k_{Hc}\kappa_M\kappa_D\kappa_G + k_{eM}k_{Mc}\kappa_H\kappa_D\kappa_G + k_{eD}k_{Dc}\kappa_H\,\kappa_M\kappa_{G+} + k_{eG}k_{Gc}\kappa_H\,\kappa_M\kappa_D, \tag{1a}$$

$$\underline{p}_c = \frac{\underline{p}_e k_{ce}}{k_{ec}}, \tag{1b}$$

$$\begin{aligned}\mathrm{H}: \underline{p}_H =\ & (k_{ec}k_{cH} + k_{ce}k_{eH} + k_{cH}k_{eH})\kappa_M\kappa_D\kappa_G \\ & + (k_{cH}k_{eD}k_{Dc} + k_{eH}k_{cD}k_{De})\kappa_M\kappa_G \\ & + (k_{cH}k_{eM}k_{Mc} + k_{eH}k_{cM}k_{Me})\kappa_D\kappa_G \\ & + (k_{cH}k_{eG}k_{Gc} + k_{eH}k_{cG}k_{Ge})\kappa_D\kappa_M,\end{aligned} \tag{1c}$$

$$\begin{aligned}\mathrm{M}: \underline{p}_M =\ & (k_{ec}k_{cM} + k_{ce}k_{eM} + k_{cM}k_{eM})\kappa_H\kappa_D\kappa_G \\ & + (k_{cM}k_{eD}k_{Dc} + k_{eM}k_{cD}k_{De})\kappa_H\kappa_G \\ & + (k_{cM}k_{eH}k_{Hc} + k_{eM}k_{cH}k_{He})\kappa_D\kappa_G \\ & + (k_{cM}k_{eG}k_{Gc} + k_{eD}k_{cG}k_{Ge})\kappa_H\kappa_D,\end{aligned} \tag{1d}$$

$$\begin{aligned}\mathrm{D}: \underline{p}_D =\ & (k_{ec}k_{cD} + k_{ce}k_{eD} + k_{cD}k_{eD})\kappa_M\kappa_H\kappa_G \\ & + (k_{cD}k_{eH}k_{Hc} + k_{eD}k_{cH}k_{He})\kappa_M\kappa_G \\ & + (k_{cD}k_{eM}k_{Mc} + k_{eD}k_{cM}k_{Me})\kappa_H\kappa_G \\ & + (k_{cD}k_{eG}k_{Gc} + k_{eD}k_{cG}k_{Ge})\kappa_M\kappa_H,\ \text{and}\end{aligned} \tag{1e}$$

$$\begin{aligned}\mathrm{G}: \underline{p}_G =\ & (k_{ec}k_{cG} + k_{ce}k_{eG} + k_{cG}k_{eG})\kappa_H\kappa_M\kappa_D \\ & + (k_{cG}k_{eH}k_{Hc} + k_{eG}k_{cH}k_{He})\kappa_M\kappa_D \\ & + (k_{cG}k_{eM}k_{Mc} + k_{eG}k_{cM}k_{Me})\kappa_H\kappa_D \\ & + (k_{cG}k_{eD}k_{Dc} + k_{eG}k_{cD}k_{De})\kappa_M\kappa_H.\end{aligned} \tag{1f}$$

The absolute probabilities p are obtained by referring the relative ones to their sum

$$\Sigma_{\underline{p}} = \underline{p}_c + \underline{p}_e + \underline{p}_H + \underline{p}_M + \underline{p}_D + \underline{p}_G, \tag{2}$$

yielding

$$\begin{aligned}p_c = \underline{p}_c/\Sigma_{\underline{p}}; p_e = \underline{p}_e/\Sigma_{\underline{p}}; p_H = \underline{p}_H/\Sigma_{\underline{p}}; \\ p_M = \underline{p}_M/\Sigma_{\underline{p}}; p_D = \underline{p}_D/\Sigma_{\underline{p}}; p_G = \underline{p}_G/\Sigma_{\underline{p}}.\end{aligned} \tag{3}$$

The particular ion currents are (e is elementary charge)

$$\mathrm{H}: I_H = e(p_c k_{cH} - p_H k_{Hc}), \tag{4a}$$

$$\mathrm{M}: I_M = e(p_c k_{cM} - p_M k_{Mc}), \tag{4b}$$

$$\mathrm{D}: I_D = 2e(p_c k_{cD} - p_D k_{Dc}), \tag{4c}$$

$$\mathrm{G}: I_G = 2e(p_c k_{cG} - p_G k_{Gc}), \tag{4d}$$

which add up to the total current

$$I = I_H + I_M + I_D + I_G. \tag{5}$$

Considering both conducting states O1 and O2 (Fig. 1 *E*), the initial current I_0 after a long dark period is exclusively mediated by the conductance of O1 ($I_0 = I_{O1}$).Then the conductance via O1 relaxes by equilibration with O2 by a factor R1, until a steady-state current I_s is reached, comprising stationary currents through both open states,

$$I_s = I_{1s} + I_{2s}, \tag{6}$$

with $I_{1S} = I_0$R1.

The reorientation of the empty binding site under the assumption of one symmetric barrier is described by the rate constants k_{ce} and k_{ec} that depend on the reduced voltage $u = EF/RT$, with the transmembrane voltage E and R, T and F having their usual thermodynamic meaning

$$k_{ec} = k_{ec}^0 \exp\left(\frac{z_E u}{2}\right), \tag{7a}$$

$$k_{ce} = k_{ce}^0 \exp\left(\frac{-z_E u}{2}\right), \tag{7b}$$

where the superscript 0 marks reference conditions ($u = 0$), z_E is the apparent charge number of the empty binding site, and the factor 1/2 in the exponent reflects a symmetric Eyring barrier.

The transfer of ionic substrates S with the charge number z_S via an intermediate binding site (c-S-e) is assumed to occur in two reversible steps in series (two symmetric barriers), which see only the portions d and $1-d$ of the total voltage, respectively:

$$k_{cS} = k^0_{cS}[S]_c \exp\left(\frac{d(z_E + z_S)u}{2}\right), \quad (8a)$$

$$k_{Sc} = k^0_{Sc} \exp\left(\frac{-d(z_E + z_S)u}{2}\right), \quad (8b)$$

$$k_{Se} = k^0_{Se} \exp\left(\frac{(1-d)(z_E + z_S)u}{2}\right), \quad (8c)$$

$$k_{eS} = k^0_{eS}[S]_e \exp\left(\frac{(d-1)(z_E + z_S)u}{2}\right). \quad (8d)$$

The voltage partitioning coefficient d (for the cytoplasmic barrier) is treated as voltage- and substrate-dependent,

$$d = \frac{(k_{Se} + k_{eS})}{(k_{Se} + k_{eS} + k_{Sc} + k_{cS})}, \quad (9)$$

and had to be iteratively determined by Eq. 8. The expressions $k_{Se} + k_{eS}$ and $k_{Sc} + k_{cS}$ in Eq. 9 are equivalent to conductances in an Ohmic voltage divider. Thus, the potential profile is not considered here as a rigid structural entity, but as an elastic one, depending on the actual voltage and substrate concentrations on both sides.

The fitting strategy was adopted from Gradmann et al. (10). Programs were written in TURBOPASCAL and are available on request. All graphs show arithmetic means and standard errors.

RESULTS

We performed electrical recordings on HEK 293 cells expressing ChR2, ChR2-LC-TC, or C1V1. The ChR2-LC-TC (CatCh+) variant with the L132C and T159C mutations was chosen because it exhibits improved retinal binding, membrane targeting, and enhanced Ca^{2+} selectivity compared to wt ChR2 (14,18–20). C1V1 was originally developed as a green-light absorbing ChR chimera to complement the color palette of optogenetic tools (14,21). The chimera approach is based on previous work where researchers have generated C1C2-hybrids to merge properties of ChR1 and ChR2 (13,22,23). The C1V1 hybrid was selected for this study because it showed an enhanced Ca^{2+} conductance in previous studies using fluorescent Ca indicators (14). We recorded $I(E)$ curves at seven different extracellular conditions for all ChR variants (see Table 1 for details of buffer composition) whereas the intracellular solution was kept at pH_c 9 with low concentrations of monovalent cations (Na^+ and K^+) to simplify the system. Internal free Ca^{2+} and Mg^{2+} were kept at 1 nM and 2 mM, respectively (24).

Fig. 2 shows typical current traces at two selected extracellular conditions. Whereas ChR2 shows a strong and rapid current decay from I_0 to I_s, this decay is smaller and slower in C1V1 and ChR2-LC-TC. The initial ChR2 current is five times higher for Na^+ at pH_e 7.2 compared to Ca^{2+} at pH_e 9 (−60 mV) whereas C1V1 and ChR2-LC-TC current sizes are only slightly reduced for Ca^{2+} at pH_e 9, suggesting a higher relative Ca^{2+} conductivity for these two variants.

For each ChR variant, three to four complete data sets were selected for further analysis. Data sets were chosen based on the consistency between pre- and postcontrol at the standard external solution (high Na^+, pH_e 7.2). Representative $I(E)$ curves at all conditions including pre- and postcontrol are shown in Fig. 3. In general, $I(E)$ curves show a moderate inward rectification. In most cases, I_s is significantly reduced compared to I_0 at high light intensities, signifying channel inactivation. However, ChR2-LC-TC hardly inactivates at less negative voltages, resulting in

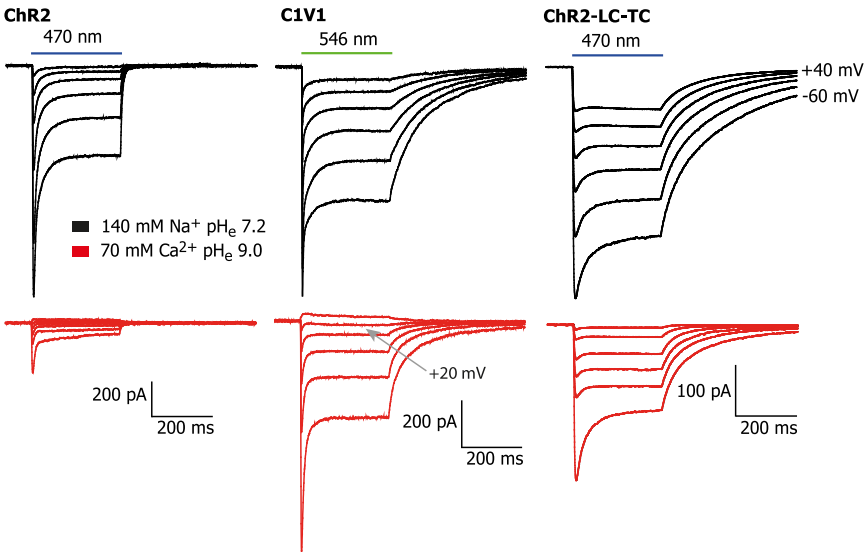

FIGURE 2 Photocurrent traces. Examples of currents for ChR2, C1V1, and ChR2-LC-TC at internal pH_c 9.0, 140 mM NMG. The voltage was varied from −60 mV to +40 mV in 20 mV steps. (*Black traces*) Currents for 140 mM external Na^+ at pH_e 7.2; (*red traces*) currents for 70 mM external Ca^{2+} at pH_e 9.0.

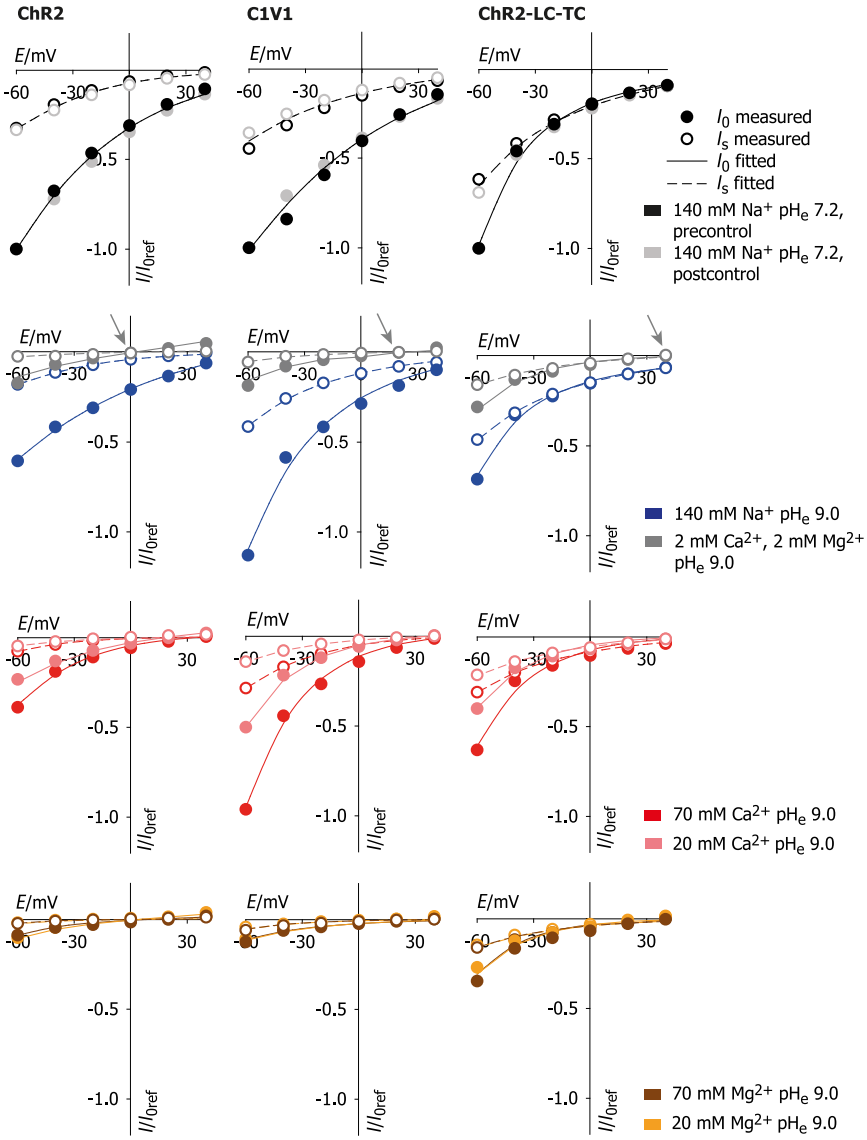

FIGURE 3 Current-voltage relationships. $I(E)$ curves for selected cells expressing ChR2, C1V1, or ChR2-LC-TC at internal NMG, pH_e 9.0. All values were normalized on the initial current amplitude I_{0ref} at standard conditions (−60 mV, 140 mM Na^+, pH_e 7.2). (*Solid circles*) Initial current amplitudes (I_0); (*open circles*) steady-state currents (I_s). (*Solid* and *dashed lines*) Corresponding fitted curves, respectively. (*Shaded arrows* in *second row*) Reversal potentials at 2 mM Ca^{2+}, 2 mM Mg^{2+}, pH_e 9.0.

almost equal current amplitudes for I_0 and I_s. Each data set was used for an independent computation of all kinetic parameters. The resulting parameters are listed in Table 2 and the corresponding fitted $I(E)$ curves are represented as lines in Fig. 3. The model-retrieved $I(E)$ curves are in good agreement with the measurements, supporting the choice of the model to sufficiently describe the data. As seen from the $I(E)$ curves in Fig. 3, ChR2-LC-TC displays more positive reversal voltages than the two other ChRs (see *shaded arrows* in *second row* for examples of reversal potentials), yielding inward currents in all presented ionic conditions and voltages, that are carried by Na^+, Ca^{2+}, Mg^{2+} or H^+. Interestingly, all variants exhibit different ion selectivities for the initial and steady-state currents. $I(E)$ curves differ most strikingly for recordings for high Ca^{2+} at pH 9 as seen from the individual recording for C1V1 in Fig. 2 showing a strong, initial inward current, but hardly any noticeable steady-state current at +20 mV.

Based on the kinetic parameters for binding and transport of each substrate, we calculated the relative contribution of the respective cations to currents in complex media. Fig. 4 illustrates the dissection of the inward currents at −60 mV at two different experimental conditions. For each condition, the slender left bar represents the initial current I_0 with the relative cation contribution. This bar reflects the ion flux through the open state O1 only provided by cells that were dark-adapted before illumination. The broader right bar corresponds to the steady-state current I_s that is fed by conductances of ChRs in both open conformations, O1 or O2. The ion selectivities of O1 and O2 slightly differ and their relative contribution depends on the variant and applied multiion electrochemical gradient. To interpret the exact composition of the inward fluxes, it is important

TABLE 2 Fitted model parameters

Cell	$CHR2_7$	$CHR2_{10}$	$CHR2_{17}$	$C1V1_1$	$C1V1_5$	$C1V1_{11}$	$TCLC_3$	$TCLC_5$	$TCLC_9$
z_{E1}	1.03	−0.92	0.06	−0.04	0.55	−0.70	−0.39	−0.54	−0.23
k_{ce1}	5.7E+2	1.3E+1	8.7E+3	3.0E+1	3.1E+2	2.3E+3	1.4E+1	1.0E+1	3.0E+3
k_{ec1}	1.8E+5	2.2E+8	3.4E+3	4.2E+3	1.4E+5	1.1E+5	9.2E+6	1.1E+8	5.4E+4
k_{cH1}	2.2E+4	2.7E+6	6.1E+5	8.1E+4	9.2E+4	8.1E+5	3.2E+6	3.3E+6	4.4E+4
k_{Hc1}	2.5E+1	1.8E0	1.1E0	8.9E−1	4.4E+1	1.8E0	2.3E+2	2.0E+2	1.9E+2
k_{He1}	2.5E+1	9.6E0	4.2E0	2.8E+1	1.3E+1	1.0E−1	3.4E−1	3.4E−1	1.1E+2
k_{cM1}	5.2E−3	3.8E−1	6.2E−2	4.3E−2	3.0E−2	1.3E−2	6.5E−1	2.0E−1	4.4E−2
k_{Mc1}	2.6E0	5.2E+1	1.2E0	3.0E+2	7.0E0	1.0E+2	2.0E+2	3.4E+2	6.0E+1
k_{Me1}	6.9E1	4.8E+2	3.8E0	4.1E+1	5.9E+1	1.0E+3	9.4E−1	1.5E+1	2.7E+1
k_{cD1}	8.9E−4	1.5E−1	2.2E−2	8.3E−3	2.0E−2	7.7E−3	2.6E−2	5.7E−2	1.1E−2
k_{De1}	2.3E−1	3.9E−1	9.2E−2	1.2E−1	1.5E−1	4.1E−1	5.8E+1	9.6E−2	1.5E−1
k_{Dc1}	2.6E+1	8.1E−1	3.7E−1	2.1E−1	3.3E0	1.5E+2	1.4E+1	3.8E−2	7.0E−1
k_{cG1}	1.5E−4	4.2E−1	3.8E−1	1.3E−2	2.6E−2	3.3E−2	3.9E−2	6.6E−2	1.9E−1
k_{Gc1}	1.7E−2	1.8E−2	1.1E−2	1.8E−1	1.2E−2	3.1E−2	7.6E−2	4.1E−2	2.8E−2
k_{Ge1}	8.8E−1	1.3E+2	1.5E0	2.0E2	2.3E0	7.4E−2	3.7E−1	1.2E−1	1.3E−1
z_{E2}	0.79	−1.11	0.82	−1.08	0.54	0.20	0.46	−0.71	−0.82
k_{ce2}	1.3E+4	8.6E0	4.4E+4	7.5E+2	3.2E+3	5.1E+3	2.9E+2	1.3E+3	1.6E+3
k_{ec2}	3.9E+3	8.9E5	2.7E+3	1.0E+4	2.9E+4	1.1E+4	5.9E+5	3.8E+4	6.3E+4
k_{cH2}	3.5E+5	4.7E+4	2.6E+5	4.9E+4	3.7E+3	1.9E+4	5.0E+4	8.2E+3	4.4E+4
k_{Hc2}	1.3E+3	9.4E+2	5.8E+2	3.7E+1	2.7E+2	6.0E0	6.7E+1	8.1E−1	2.1E+2
k_{He2}	4.4E+1	1.5E+2	4.0E+1	3.1E+1	3.7E−1	1.9E−1	1.1E0	2.3E+1	3.6E+1
k_{cM2}	4.7E−1	1.5E−2	1.9E−1	1.2E−1	8.0E−2	2.2E−3	3.0E−2	7.2E−3	4.5E−2
k_{Mc2}	2.3E+3	1.3E+2	7.6E+2	6.2E+1	8.4E+1	7.3E0	1.1E+4	9.7E+1	8.1E+1
k_{Me2}	4.8E+1	5.9E0	3.0E+1	1.2E0	1.2E+1	5.3E1	3.7E+2	2.2E+2	1.4E+1
k_{cD2}	5.4E−3	3.0E−4	2.0E−3	9.9E−4	7.2E−3	3.0E−3	2.2E−3	5.5E−1	2.4E−2
k_{De2}	2.6E−3	3.3E−1	3.6E−3	2.0E−1	9.1E−2	6.3E−2	3.2E0	2.0E−1	1.4E−1
k_{Dc2}	1.5E−2	2.9E−4	1.0E−1	2.6E−1	6.0E−1	1.2E−1	1.6E0	7.3E−4	4.0E−2
k_{cG2}	7.5E−3	9.2E−4	9.1E−4	7.3E−4	1.1E−1	4.5E−4	2.1E−3	1.0E−2	8.6E−2
k_{Gc2}	1.1E−3	1.8E−2	9.9E−4	6.2E−4	5.0E−3	1.3E−2	1.3E−2	7.1E−3	3.0E−2
k_{Ge2}	1.2E−3	8.6E0	1.4E−2	1.2E+2	1.7E−1	5.8E−2	2.4E−2	3.1E0	5.7E−2
R_1	0.088	0.081	0.126	0.373	0.024	0.152	0.53	0.36	0.007
Error	0.057	0.072	0.028	0.116	0.079	0.052	0.066	0.035	0.029

Fitted model parameters (see Fig. 1, *D* and *E*) of analyzed cells. z_{Ek}, apparent charge of the empty binding site in conducting state O_k ($k = 1, 2$); k_{ijk}, rate constants (s^{-1}) from state *i* to state *j* of conducting state O_k at reference conditions (zero voltage and 1 mM substrate concentrations at both sides), normalized to reference current I_{0ref} at external 140 mM Na^+, pH_e 7.2 and internal NMG, pH_c 9.0 and −60 mV; and *R*, steady-state portion of current through state O1 compared to instantaneous current. Indices reflect respective substrates: H, protons; M, Na^+ or K^+; D, Ca^{2+}; G, Mg^{2+}.

to remember that the internal solution was kept at low Na^+, very low Ca^{2+}, and pH_c 9.0, which does not represent the physiological intracellular composition in mammalian cells with typically high K^+, nanomolar Ca^{2+}, and pH 7.4. Furthermore, the applied voltage for the data in Fig. 4 was −60 mV, meaning that the conditions were far from thermodynamic equilibrium.

Of the three ChRs tested, ChR2 shows the highest degree of inactivation. Inactivation is lower in C1V1 and lowest in ChR2-LC-TC. The high contribution of O2 to the steady-state current of ChR2-LC-TC as seen from Fig. 4 *A* may at least partially account for its low inactivation. Notably, ChR2-LC-TC displays a high Mg^{2+} conductance (*yellow* and *orange bars*), which is further discussed below. At high Na^+ and pH_e 7.2 the initial currents are mostly carried by H^+ whereas steady-state currents have a higher contribution of Na^+ resulting from a higher relative Na^+ conductivity of O2 at least at this voltage. Contribution from Ca^{2+} and Mg^{2+} are generally low because there is a high driving force for Na^+ and H^+ influx, both of which compete for transport with Ca^{2+} and Mg^{2+}. The situation is quite different at 70 mM Ca^{2+}, pH_e 9.0 (Fig. 4 *B*). At this specific condition, the driving force is highest for Ca^{2+} influx and currents of all variants are mainly carried by Ca^{2+} with only minor contributions from other ions. Again, contribution of H^+ is smaller in O2 than O1, leading to a lower relative contribution of H^+ and a higher relative contribution of Ca^{2+} to all steady-state currents.

For a closer insight into the Ca^{2+} and Mg^{2+} conductance of ChRs, current amplitudes at three different Ca^{2+} and Mg^{2+} concentrations were analyzed. Current contributions of these two substrates to the total current—so-called partial currents I_p—were calculated and plotted against the respective substrate concentration (Fig. 5). By application of the Michaelis-Menten algorithm K_m and V_{max} values for Ca^{2+} and Mg^{2+} transport were determined (Table 3). Evidently, the respective K_m values are small for Mg^{2+} transport and larger for Ca^{2+}. Moreover, the V_{max} values are higher for Ca^{2+} than for Mg^{2+} and differ significantly between the different ChR variants. Whereas C1V1 exhibits the highest

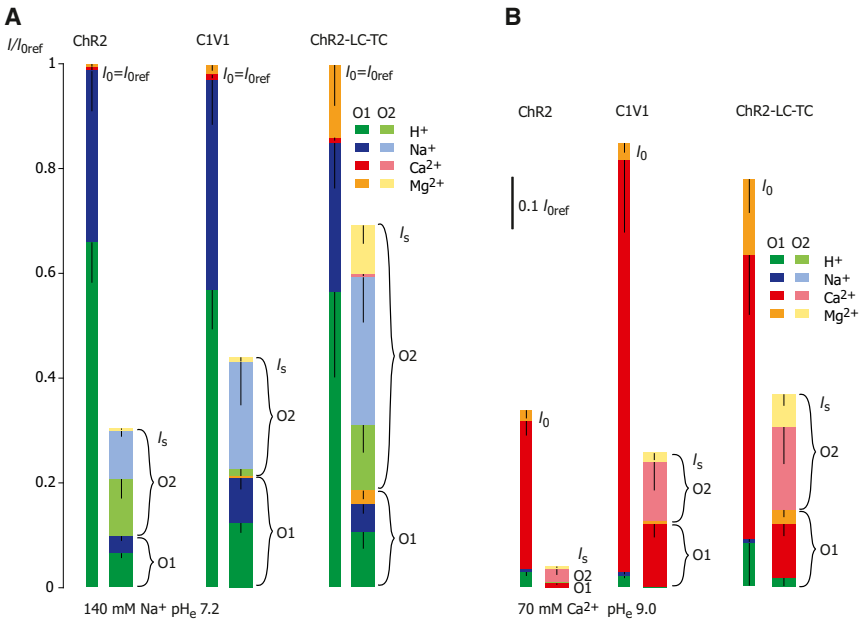

FIGURE 4 Ionic composition. Dissection of inward currents into contribution of different competing ion species at internal NMG, pH_c 9.0 and −60 mV. The external solutions were kept at 140 mM Na^+, pH_e 7.2 (*A*) and at 70 mM Ca^{2+}, pH_e 9.0 (*B*). (*Slender bars* in *dark colors*) Initial currents (I_0) that are only made up by O1. (*Broad bars*) Steady-state currents (I_s) composed of currents through both O1 (*dark color*) and O2 (*light color*). (*Vertical solid lines*) Standard errors of individual partial currents.

Ca^{2+}-mediated initial current, ChR2-LC-TC shows an even higher Ca^{2+}-based steady-state current than C1V1 (14). As mentioned above, ChR2-LC-TC shows large Mg^{2+} currents, which is true for both initial and late current, and is reflected by its high V_{max} values for Mg^{2+} transport. For all variants tested, Mg^{2+} has a larger affinity and smaller conductance compared to Ca^{2+}.

All ion contributions shown so far were calculated from data sets at experimentally verified conditions. However, the model allows predictions for ion conductance at conditions that were not experimentally tested. For 70 mM Ca^{2+} at pH_e 7.2, the current sizes and contributions by different ions were calculated from the model parameters gained from the seven standard conditions (Fig. 6 *A*). The model predicts a high H^+ conductance, especially for the early current I_0. Interestingly, the partial currents for Ca^{2+} at pH_e 7.2 are lower than the Ca^{2+} currents at pH_e 9 (Fig. 4 *B*) indicating a suppression of Ca^{2+} transport by competition with protons. Whereas this H^+ competition seems strongest in wt ChR2, steady-state currents of C1V1 and ChR2-LC-TC are less affected by the decrease of external pH. To validate the predicted current sizes, the current amplitudes at 70 mM Ca^{2+}, pH_e 7.2 were empirically measured (Fig. 6 *B*). Strikingly, the measured total currents coincide well with the ones predicted by the model. Moreover, the amplitude differences between the different ChR variants could be experimentally reproduced, and the model seems appropriate for predicting current amplitudes and ion composition under widely different conditions. We recommend this approach for calculation of the ion composition of photocurrents at conditions with several competing ions.

DISCUSSION

Early studies established that ChRs conduct protons, different monovalent cations (Li^+, Na^+, K^+, Cs^+), as well as Ca^{2+} and Mg^{2+} in host cells (2,10). However, the contribution of the different ions in a complex medium to the photocurrent remained unknown. This led to quite controversial discussions about the preferences of ChR-variants under widely different experimental conditions. The reason is that the current of a specific ion species depends on the electrochemical gradient across the membrane, the competition for binding and transport with other cations, and the conformational states of the individual ChR molecules

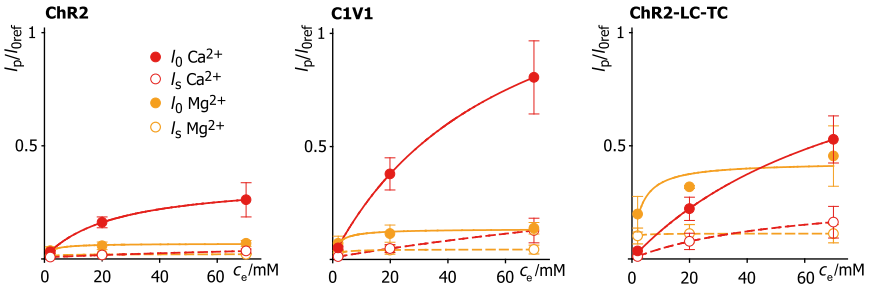

FIGURE 5 Ca^{2+} and Mg^{2+} titration. Normalized partial Ca^{2+} and Mg^{2+} currents I_p at different external substrate concentrations normalized to standard conditions (140 mM Na^+, pH_e 7.2). Partial currents were calculated from $I(E)$ relationships and plotted against the respective substrate concentration. (*Solid circles*) I_0; (*open circles*) I_s. (*Lines*) Fits based on Michaelis-Menten kinetics.

TABLE 3 Ca^{2+} and Mg^{2+} titration parameters

	Calcium				Magnesium			
	Initial		Stationary		Initial		Stationary	
	$I_{max0}/\%I_{0ref}$	K_{M0}/mM	$I_{maxs}/\%\ I_{0ref}$	K_{Ms}/mM	$I_{max0}/\%\ I_{0ref}$	K_{M0}/mM	$I_{maxs}/\%I_{0ref}$	K_{Ms}/mM
ChR2								
Cell 7	45	24	0.68	43	10	180	1.0	1.5
Cell 10	132	240	3.5	44	8.8	0.2	1.8	2.6
Cell 15	42	51	14	140	7.8	2.7	1.6	3.3
Cell 17	35	18	11	220	7.6	2.3	1.3	2.5
C1V1								
Cell 1	92	66	6.8	226	28	138	0.1	2.3
Cell 5	204	75	239	794	18	1.3	6.9	1.5
Cell 11	176	70	19	52	11	1.0	3.9	2.3
ChR2-LC-TC								
Cell 3	68	21	3.8	74	120	60	2.7	0.7
Cell 5	103	69	50	64	33	0.5	14	0.17
Cell 9	92	140	37	66	31	0.2	16	0.3

Numerical results of maximum current, I_{max}, and half-maximum ion concentration, K_M, for partial Ca^{2+} and Mg^{2+} currents at −60 mV and pH_e 9.0 for individual cells investigated. Values determined by MM linear regression from three data points at 2, 20, and 70 mM, respectively.

that depend on the intensity and duration of the applied light. Here we used an enzyme-kinetic model to quantitatively describe ion transport of four different substrates via two different open channel conformations O1 and O2. We applied the model to experimental data from three ChR variants that are of special interest for optogenetic applications.

Some general conclusions can be drawn from our data. First, at pH_e 7.2, proton-mediated inward currents are large and sensitive to the presence of competing ions such as Na^+ and Ca^{2+}. Interestingly, although protons inhibit inward Na^+ and Ca^{2+} currents, partial Mg^{2+} currents seem unaffected by the external proton concentration, which is interpreted to indicate strong Mg^{2+} binding, and is reflected by

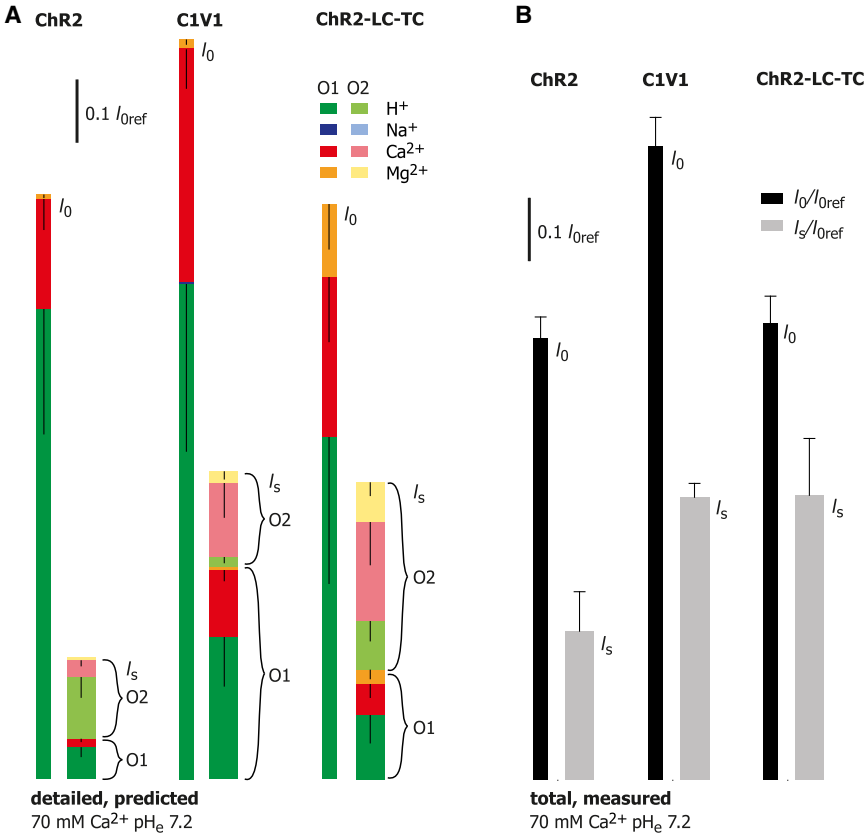

FIGURE 6 Comparison of current prediction and experimental values. (*A*) Predicted contribution of different ion species to I_0 and I_S at −60 mV, calculated for an internal solution of 140 mM NMG, pH_c 9 and external solution of 70 mM Ca^{2+}, pH_e 7.2. (*B*) Experimental confirmation of the total current amplitudes under the same conditions.

the small K_m values for Mg^{2+} transport. At −60 mV, the relative contribution of protons to the current is larger when ChRs are in the O1 state compared to the O2 state (Figs. 4 *A* and 6 *A*) resulting in a high proton conductance of the initial current I_0. At first glance, this finding seems to contradict our earlier claim of "progressive proton selectivity" with time (9). However, the earlier studies considered reversal voltages representing conditions close to equilibrium, whereas this study is mainly focused on conditions with a high driving force for inward currents; i.e., far from equilibrium. Fig. 7 illustrates the observed change in the reversal voltage for ChR2 when the extracellular pH is decreased from pH_e 9.0 to 7.2. At pH_c 7.2, this shift is significantly larger for the steady-state current I_s compared to the initial current I_0, confirming a higher proton selectivity of I_s as reported by Berndt et al. (9). Thus, the selectivity pattern of a channel in physiological conditions may significantly differ from the pattern derived from reversal voltages. In principle, this distinction of the selectivity near and far from equilibrium corresponds to the familiar distinction of K_M- and V_{max}-relations in conventional Michaelis-Menten kinetics.

Here, cytoplasmic conditions of low internal Na^+, pH_c 9.0, were chosen to minimize outward currents, which allowed for the reduction of the number of free parameters by combining intracellular binding and transport into one reversible step. In contrast, physiological conditions of high K^+, pH_c 7.4, will cause smaller proton-driven inward currents (Figs. 4 and 6). Nevertheless, researchers using ChRs should keep in mind that ChRs exhibit considerably high proton conductivity even at physiological conditions, which may cause some intracellular acidification accompanying membrane depolarization.

Furthermore, the choice of the right mutant for a specific optogenetic experiment is crucial because different ChRs differ in their respective current profiles and ion selectivities. ChR2 (H134R) has been the predominant optogenetic tool to date, but this variant bears major disadvantages compared to recently developed and optimized ChRs. Most importantly, at neutral pH_c both ChR2 and the H134R variant display large I_0/I_s-ratios thus disabling sustained membrane depolarization (Figs. 2–4 and 6). In addition, inhibition of both Na^+ and Ca^{2+} inward currents by competing protons is strong in ChR2, yielding small relative Na^+ and Ca^{2+} inward currents and high proton currents (Fig. 4 *A*) that may result in intracellular acidification. In contrast, C1V1 shows smaller I_0/I_s ratios than ChR2 and the I_0/I_s for ChR2-LC-TC is almost unity, especially at positive voltages. Moreover, proton conductance and therefore proton competition with other ions are less pronounced in these two variants. Whereas Ca^{2+} driven initial currents are highest in C1V1, ChR2-LC-TC is best suited when a sustained Ca^{2+} influx is required. Interestingly, Mg^{2+} transport is high in ChR2-LC-TC even at low extracellular Mg^{2+} concentration (2 mM), which should be taken into account whenever ChR2-LC-TC is applied. Earlier studies promoted C1V1 and ChR2-LC-TC because both ChRs share the cysteine at position 159 (C198 in C1V1) that was described to enhance protein stability and retinal binding (18,20). Besides the channel properties discussed here, other qualities such as kinetic parameters and wavelength of the actinic light should be taken into account for choosing ChRs for applications (14,25).

CONCLUSIONS

A model based on enzyme kinetics allowed us to dissect ChR currents into contributions by different competing cations and predict current sizes at electrochemical conditions that were not experimentally tested. The model may contribute to understanding the molecular basis for ion transport via two open conformations that show distinct ion binding and transport rates. For a deeper molecular insight into ChR activation, a three-dimensional structure of at least one of the open conformations would be advantageous.

We thank Altina Klein and Maila Reh for excellent technical support.

This research was supported by the German Research Foundation (Deutsche Forschungsgemeinschaft grant Nos. HE3824/9-4, FOR-1279:HE3824/21-1, and SFB-1078/B2 to P.H.).

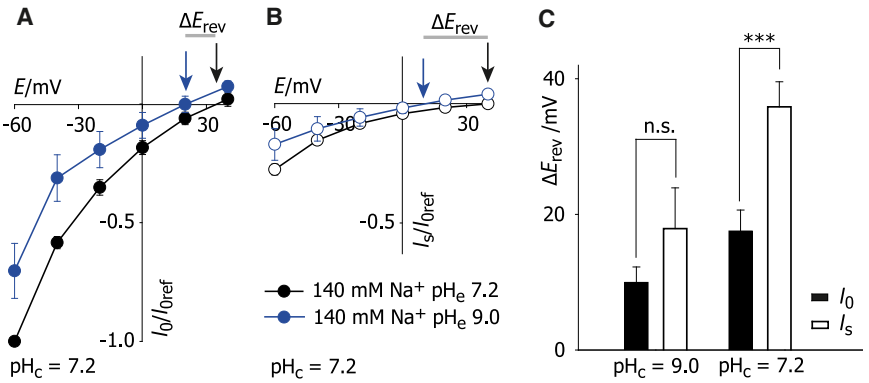

FIGURE 7 Reversal voltages. (*A* and *B*) *I*(*E*) plots of the initial current I_0 (*A*) and the steady-state current I_S (*B*) at 140 mM Na^+, pH_e 9 and 140 mM Na^+, pH_e 7.2 both at internal pH_c 7.2. The shift in the reversal potential is significantly higher for I_s than for I_0. (*C*) Shift of reversal potentials between 140 mM Na^+, pH_e 9 and 140 mM Na^+, pH_e 7.2 at two different intracellular pH_c conditions.

REFERENCES

1. Nagel, G., D. Ollig, …, P. Hegemann. 2002. Channelrhodopsin-1: a light-gated proton channel in green algae. *Science.* 296:2395–2398.
2. Nagel, G., T. Szellas, …, E. Bamberg. 2003. Channelrhodopsin-2, a directly light-gated cation-selective membrane channel. *Proc. Natl. Acad. Sci. USA.* 100:13940–13945.
3. Boyden, E. S., F. Zhang, …, K. Deisseroth. 2005. Millisecond-timescale, genetically targeted optical control of neural activity. *Nat. Neurosci.* 8:1263–1268.
4. Li, X., D. V. Gutierrez, …, S. Herlitze. 2005. Fast noninvasive activation and inhibition of neural and network activity by vertebrate rhodopsin and green algae channelrhodopsin. *Proc. Natl. Acad. Sci. USA.* 102:17816–17821.
5. Nagel, G., T. Szellas, …, E. Bamberg. 2005. Channelrhodopsins: directly light-gated cation channels. *Biochem. Soc. Trans.* 33:863–866.
6. Hegemann, P., S. Ehlenbeck, and D. Gradmann. 2005. Multiple photocycles of channelrhodopsin. *Biophys. J.* 89:3911–3918.
7. Nikolic, K., P. Degenaar, and C. Toumazou. 2006. Modeling and engineering aspects of channelrhodopsin2 system for neural photostimulation. *IEEE Eng. Med. Biol. Soc.* 1:1626–1629.
8. Nikolic, K., N. Grossman, …, P. Degenaar. 2009. Photocycles of channelrhodopsin-2. *Photochem. Photobiol.* 85:400–411.
9. Berndt, A., M. Prigge, …, P. Hegemann. 2010. Two open states with progressive proton selectivities in the branched channelrhodopsin-2 photocycle. *Biophys. J.* 98:753–761.
10. Gradmann, D., A. Berndt, …, P. Hegemann. 2011. Rectification of the channelrhodopsin early conductance. *Biophys. J.* 101:1057–1068.
11. Gradmann, D., and C. M. Boyd. 2005. Apparent charge of binding site in ion-translocating enzymes: kinetic impact. *Eur Biophys J.* 34:353–357.
12. Zhang, F., M. Prigge, …, K. Deisseroth. 2008. Red-shifted optogenetic excitation: a tool for fast neural control derived from *Volvox carteri*. *Nat. Neurosci.* 11:631–633.
13. Tsunoda, S. P., and P. Hegemann. 2009. Glu 87 of channelrhodopsin-1 causes pH-dependent color tuning and fast photocurrent inactivation. *Photochem. Photobiol.* 85:564–569.
14. Prigge, M., F. Schneider, …, P. Hegemann. 2012. Color-tuned channelrhodopsins for multiwavelength optogenetics. *J. Biol. Chem.* 287:31804–31812.
15. Bamann, C., R. Gueta, …, E. Bamberg. 2010. Structural guidance of the photocycle of channelrhodopsin-2 by an interhelical hydrogen bond. *Biochemistry.* 49:267–278.
16. Klieber, H. G., and D. Gradmann. 1993. Enzyme kinetics of the prime K^+ channel in the tonoplast of Chara: selectivity and inhibition. *J. Membr. Biol.* 132:253–265.
17. King, E. L., and C. Altman. 1956. A schematic method of deriving the rate laws for enzyme-catalyzed reactions. *J. Phys. Chem.* 60:1375–1378.
18. Berndt, A., P. Schoenenberger, …, T. G. Oertner. 2011. High-efficiency channelrhodopsins for fast neuronal stimulation at low light levels. *Proc. Natl. Acad. Sci. USA.* 108:7595–7600.
19. Kleinlogel, S., K. Feldbauer, …, E. Bamberg. 2011. Ultra light-sensitive and fast neuronal activation with the Ca^{2+}-permeable channelrhodopsin CatCh. *Nat. Neurosci.* 14:513–518.
20. Ullrich, S., R. Gueta, and G. Nagel. 2012. Degradation of channelopsin-2 in the absence of retinal and degradation resistance in certain mutants. *Biol. Chem.* 394:271–280.
21. Yizhar, O., L. E. Fenno, …, K. Deisseroth. 2011. Neocortical excitation/inhibition balance in information processing and social dysfunction. *Nature*. 477:171–178.
22. Wang, H., Y. Sugiyama, …, H. Yawo. 2009. Molecular determinants differentiating photocurrent properties of two channelrhodopsins from *Chlamydomonas*. *J. Biol. Chem.* 284:5685–5696.
23. Lin, J. Y., M. Z. Lin, …, R. Y. Tsien. 2009. Characterization of engineered channelrhodopsin variants with improved properties and kinetics. *Biophys. J.* 96:1803–1814.
24. Schoenmakers, T. J., G. J. Visser, …, A. P. Theuvenet. 1992. CHELATOR: an improved method for computing metal ion concentrations in physiological solutions. *Biotechniques.* 12:870–874, 876–879.
25. Mattis, J., K. M. Tye, …, K. Deisseroth. 2012. Principles for applying optogenetic tools derived from direct comparative analysis of microbial opsins. *Nat. Methods.* 9:159–172.